Liquid-Phase Synthesis, Sintering, and Transport Properties of Nanoparticle-Based Boron-Rich Composites

Guillaume Gouget, Damien Bregiroux, Rémi Grosjean, David Montero, Stefan Maier, Franck Gascoin, Clément Sanchez, David Portehault

▶ **To cite this version:**

Guillaume Gouget, Damien Bregiroux, Rémi Grosjean, David Montero, Stefan Maier, et al.. Liquid-Phase Synthesis, Sintering, and Transport Properties of Nanoparticle-Based Boron-Rich Composites. Chemistry of Materials, 2021, 33 (6), pp.2099-2109. 10.1021/acs.chemmater.0c04762 . hal-03214780

HAL Id: hal-03214780

https://hal.sorbonne-universite.fr/hal-03214780

Submitted on 2 Sep 2021

HAL is a multi-disciplinary open access archive for the deposit and dissemination of scientific research documents, whether they are published or not. The documents may come from teaching and research institutions in France or abroad, or from public or private research centers.

L'archive ouverte pluridisciplinaire **HAL**, est destinée au dépôt et à la diffusion de documents scientifiques de niveau recherche, publiés ou non, émanant des établissements d'enseignement et de recherche français ou étrangers, des laboratoires publics ou privés.

Liquid-Phase Synthesis, Sintering, and Transport Properties of Nanoparticle-Based Boron-Rich Composites

Guillaume Gouget, Damien Bregiroux, Rémi Grosjean, David Montero, Stefan Maier, Franck Gascoin, Clément Sanchez, and David Portehault*

ABSTRACT: Nanostructuring boron-rich materials should significantly impact their thermal and electrical transport properties. Nonetheless, nanostructured monoliths of such materials could not be achieved in the 10 nm range so far, because of the large temperatures required to synthesize and produce boron-rich compounds. Such a nanostructuration may have important consequences for achieving a trade-off between enhanced electrical and low thermal conductivity in boron-rich materials, which are among the few materials enabling thermoelectric power generation above 1000 K thanks to their thermal stability, high positive Seebeck coefficients, and low thermal conductivity. In this study, we use a one-pot synthesis in inorganic molten salts to yield a nanocomposite consisting of metallic HfB_2 nanocrystals dispersed in an insulating amorphous boron-rich matrix with a controlled volume fraction of nanocrystals from 16 to 56 vol %. We show that this controlled liquid-phase synthesis can be coupled to spark plasma sintering for densification preserving the nanostructure. The relationships between the reagent ratio in the liquid-phase synthesis, sintering conditions, and transport properties of the densified nanocomposites are then highlighted. We then design materials exhibiting metallic electrical conductivity related to the HfB_2 nanocrystals, together with enhanced thermal dissipation attributed to the nanostructured amorphous boron matrix. Combined with the versatility offered by in-solution routes toward boride-based nanocomposites, this work opens a new avenue for tuning transport properties in boron-rich nanomaterials.

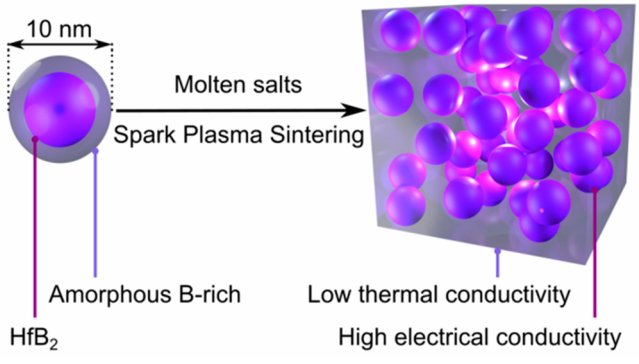

INTRODUCTION

Mastering simultaneously and independently thermal and electrical transport properties of materials is one central challenge underlying the design of thermoelectric materials. Overcoming this challenge is paramount in order to recover heat losses in transportation and industry[1] and to complement energy conversion technologies such as photovoltaics.[2] Nanostructuring thermoelectrics has enabled a significant increase in their performances,[3] because it can minimize thermal conductivity without significantly impacting electrical conductivity, by lowering the contribution of phonons.[4−8] This effect has been observed in many nanostructured materials targeting thermoelectric energy conversion at room temperature (RT)[9−11] and up to approximately 700 K.[12−14] Much fewer studies address materials able to operate above 1000 K, and they focus only on silicon nanostructured thermoelectrics.[15] Combining materials with different properties at a length scale below 100 nm is one way to independently optimize thermal and electrical behaviors.[11,16−18] Such nanocomposites were produced by using a conductive matrix embedding a variety of nanoparticles, like bismuth and antimony tellurides,[11] tellurium,[19] or polymers[20] operating at temperatures well below 1000 K. Very few nanocomposites able to operate above 1000 K have been reported so far.[16] They are built from Si-based materials.[16] Their fabrication is challenging due to the high temperatures required for processing and because the number of thermoelectric materials which are stable at such high temperatures is very limited, encompassing $Si_{1-x}Ge_x$,[21,22] $Yb_{14}MnSb_{11}$,[23] $Yb_{4-x}Sm_xSb_3$,[24,25] $La_{3-x}Te_4$,[26] $B_{6.5}C$,[27] and $Ca_{0.5}Sr_{0.5}B_6$.[28,29] Boron-rich materials are pertinent candidates for high-temperature thermoelectric energy conversion because of their refractory properties and their high Seebeck coefficients.[30−35] High temperature gradients (approximately 2000 K for boron carbides, for instance) can be applied, and consequently high thermoelectric efficiencies can be obtained (e.g., η = 25% for boron carbides),[36] despite modest figures of merit. Among boron-

rich solids, boron carbides are p-type conductors and alkaline earth metal hexaborides are n-type ones,[28,29] both addressing the need for p- and n-type materials in thermoelectric devices. Nonetheless, their transport properties, including the nature of charge carriers, can hardly be controlled. Hence, new boron-based materials should be investigated for their thermoelectric properties with controlled charge carrier type.

The electrical and thermal transport properties of boron-based microstructured composites have been scarcely assessed,[37,38] and no study has been reported on the transport properties of nanostructured boron-rich materials and on their nanocomposites. This is due to two obstacles: the scarcity of synthesis strategies toward B-rich compositions at the nanoscale[39−41] and the difficulty to process these materials.[42]

The obstacle of the synthesis of nanostructured boron-rich solids is addressable by liquid-phase synthesis. Indeed, the formation of metal borides in inorganic salt melts[43] yields nanocrystals with controlled sizes generally below 20 nm and adjustable compositions with various metals and metal-to-boron stoichiometries (Figure 1).[40,43,44] This one-step synthesis systematically yields metal boride nanocrystals embedded in an amorphous boron-rich shell. This shell is prone to structural evolution when exposed to different atmospheres, temperatures, and pressures.[45,46] Therefore, it should be possible to design innovative nanocomposites encompassing the metal boride nanocrystals and a surrounding matrix resulting from the initial shell.

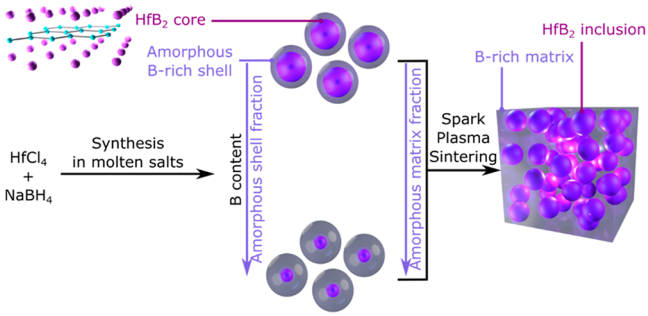

Figure 1. Scheme of the coupling process between synthesis of HfB_2 nanocrystals in molten salts for the controlled composition of core−shell nanoparticles and spark plasma sintering for producing monoliths embedding conductive nanocrystals. In the HfB_2 crystal structure, top left, B and Hf atoms are light blue and purple, respectively.

The second obstacle relates to processing and is linked to the difficulty to sinter boron-rich compounds, which are refractory materials built on strong and directional covalent bonds. The high temperatures required for conventional sintering usually result in large grain sizes and loss of nanoscale features.[47] Spark plasma sintering (SPS) can overcome this limitation (Figure 1). It relies on pulsed current-based heating through the Joule effect in the sample and a graphite die. Because of the local heating, high heating rates are achieved and accompanied by efficient sintering at a lower temperature and shorter time compared to other hot-pressing techniques. These are key advantages to maintaining the nanostructure of materials.[48−51] SPS can be adapted to the densification of ultrahard and refractory materials such as ZrB_2 and HfB_2.[37,52−54] Composites of yttrium borides doped with various p-block elements were also obtained by reactive SPS in previous works, where a chemical reaction occurred during sintering.[47,55−57] Nonetheless, SPS has never been applied to target boron-rich composites nanostructured at the 10 nm-length scale.

In the present work, we combine the synthesis in inorganic molten salts and spark plasma sintering to design nanocomposites (Figure 1) consisting of a dispersion of metallic HfB_2 nanocrystals embedded in an insulating, amorphous boron-based matrix. The inclusion size and the volume fraction can be tuned, allowing a fine adjustment of the balance between the conductive and the insulating components. By enabling the decoupling between electrical and thermal transport, nanostructuration provides access to new multiphasic boron-rich materials with adjustable transport properties.

RESULTS AND DISCUSSION

Controlling the Volume Fraction in HfB_2−Boron Core−Shell Nanoparticles from Molten Salts. The synthesis of HfB_2 core−shell nanoparticles in inorganic molten salts was adapted from previous studies.[43] Briefly, various masses of LiCl, KCl, $HfCl_4$, and $NaBH_4$ anhydrous powders were ground and mixed together under an argon atmosphere (Table S1). The reaction mixtures were heated to 900 °C during 4 h and then cooled to room temperature (RT). The salts were dissolved in deionized water, and the resulting black powders were washed by successive steps of centrifugation and redispersion in deionized water. The samples were dried in a vacuum at 60 °C. Before studying the effect of a change in the boron precursor proportion relative to hafnium, typical morphological and structural features of the products are described in Figure 2, starting with 2.00 mmol of $HfCl_4$ and 8.00 mmol of $NaBH_4$ (Hf:B molar ratio of 1:4). Transmission electron microscopy (TEM) data show that the powder encompasses polycrystalline aggregates (Figure 2a) presenting a selected area electron diffraction (SAED) pattern, which can be fully indexed according to the HfB_2 structure (*P6/mmm*). These aggregates are composed of spherical core−shell nanoparticles (Figure 2b). The core is made of an HfB_2 single crystal, as confirmed by high-resolution TEM (Figure 2c). The shell is amorphous and appears with a brighter contrast associated with a lower concentration of the heavy element hafnium compared to the core. The amorphous shell is continuous between two HfB_2 nanocrystals, suggesting that the core−shell nanoparticles are irreversibly bound together. Energy-dispersive X-ray spectrometry (EDS) performed in a scanning electron microscope (SEM) indicates that hafnium, boron, and oxygen are the only elements detected, with an overall composition $Hf_{0.2}B_{0.6}O_{0.2}$ (Figure S1). Oxygen was reported to occur from the washing step with deionized water.[43] No element from the inorganic solvent (neither chlorine nor any alkali element) is detected. The Hf:B molar ratio of 0.31(3) from EDS is confirmed by the value of 0.36(2) obtained by ICP-OES. Both elemental analysis techniques confirm an excess of boron, in comparison to the nominal HfB_2 stoichiometry. This boron excess (noted B_{am}) and the presence of oxygen account for the amorphous shell.[43,58] The experimental ratio $O:B_{am}$ is calculated from EDS data, after subtracting the B content involved in HfB_2. The $O:B_{am}$ ratio is 0.7(2), which is lower than the O:B ratio of 1.5 in fully oxidized B_2O_3, indicating that boron is only partially oxidized in the shell.[43,45,46]

The initial Hf:B was varied from 1:3, i.e., 1.5 equiv of boron compared to the stoichiometry in HfB_2, to 1:12, corresponding

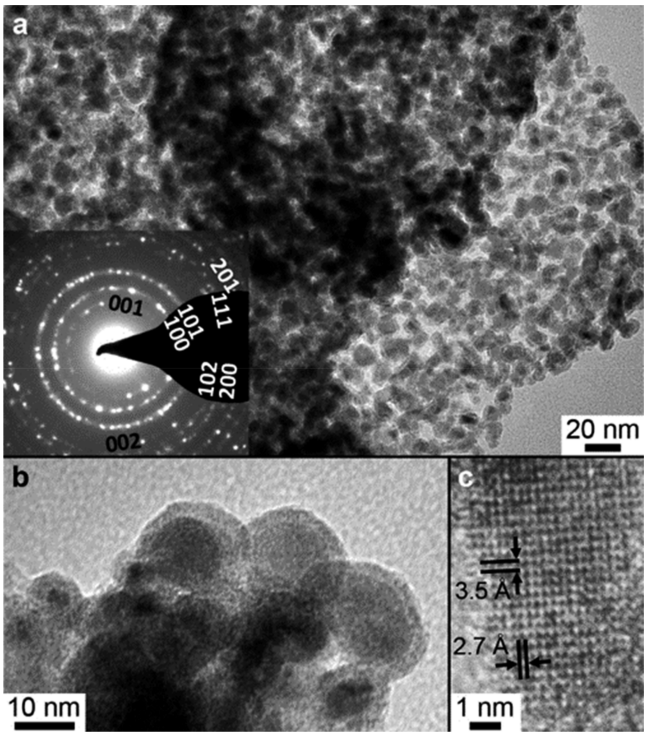

Figure 2. TEM micrographs of the HfB_2-based nanocomposite obtained with an initial Hf:B molar ratio of 1:4. (a) Aggregate of nanoparticles and corresponding SAED (inset) pattern indexed according to the HfB_2 structure. (b) Core–shell nanoparticles with the HfB_2 core with higher contrast than the boron-rich shell. (c) HRTEM micrograph of a core with periodical ordering related to (001) and (100) (zone axis [010]) interreticular planes with 3.5 and 2.7 Å spacings, respectively.

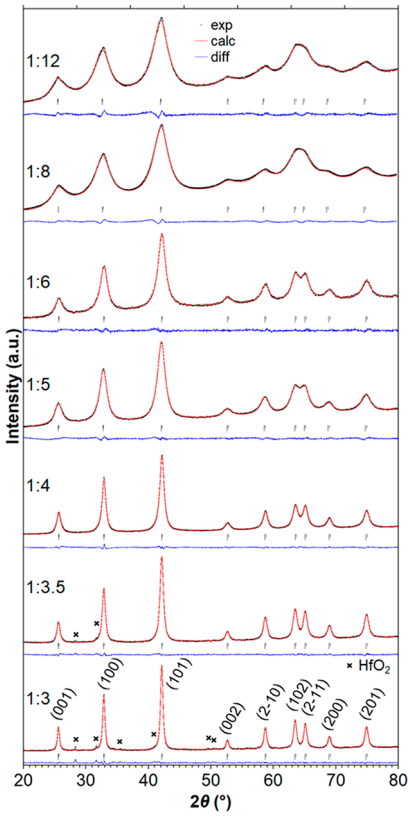

Figure 3. XRD patterns and Le Bail refinements of nanocrystalline HfB_2 for various hafnium-to-boron molar ratios (Hf:B) of precursors initially introduced. Calculated reflections for HfB_2 are indicated with vertical lines below diagrams.

to 6 equiv. Hereafter, samples are named according to the initial Hf:B molar ratio. Powder XRD patterns (Figure 3) show that HfB_2 is the only phase detected for samples 1:4, 1:5, 1:6, 1:8, and 1:12. For lower boron contents, a minor hafnium dioxide contamination is observed. Refined cell parameters of HfB_2 are close to the reported values (Table S2) and do not depend significantly on the crystal size. The broadness of all HfB_2 reflections increases with the initial boron concentration, which is associated with the decrease in the HfB_2 apparent crystallite and particle size, as previously observed by TEM for Hf:B ratios of 1:4 to 1:12.[40] The same trend is observed for Hf:B ratios of 1:3 and 1:3.5 (Figure S2). Therefore, the HfB_2 particle size can be tuned through the initial concentration of the boron precursor, borohydride. The average diameter of the core and the average thickness of the shell measured by TEM pictures (Figure S2) are plotted in Figure 4a as a function of the initial Hf:B molar ratio. For samples with a ratio between 1:3 and 1:12, the average core diameter is divided by about five from 13.0 to 2.3 nm, whereas the shell thickness decreases only by approximately 30%. As a result, the volume fraction of HfB_2 (noted ρ) decreases (Figure 4b) with the Hf:B = 1:n ratio (increasing n), from 56% for sample 1:3 to 16% for 1:12. Hence, adjusting the boron precursor concentration enables tuning the volume fraction of metal boride in the amorphous partially oxidized boron matrix.

The two components of the nanocomposites formed by the synthesis in molten salts bear very different transport properties. Indeed, bulk HfB_2 is a metallic conductor,[52,59] while the shell consists of partially oxidized amorphous boron.[43,46] Related materials such as crystalline boron (β-B) and boron oxide glasses are electrical insulators with a low thermal conductivity, and β-B has a high Seebeck coefficient.[60,61] We took advantage of the control of the composition and nanostructure to study how the transport properties of these nanocomposites are affected by changes in HfB_2 crystal size. Considering a monodisperse assembly of spheres, the theoretical three-dimensional percolation threshold corresponds to the volume fraction $\rho_{thr.}$ = 34 vol %.[62] Among the samples studied, the HfB_2 volume fraction of 33 vol % in sample 1:6 is the closest to ρ_{thr}. Hence, we have focused our study on samples 1:4 and 1:6, corresponding to 41 and 33 vol % of conductive nanocrystals, i.e., well above and close to the percolation threshold, respectively. To achieve high densities while keeping the nanostructure of the composites unchanged, spark plasma sintering was favored over conventional hot-pressing for its ability to deliver homogeneous sintered monoliths that maintain the nanocrystalline particles within the nanocomposite.[48−51]

Densification by Spark Plasma Sintering. Sintering temperatures and pressures were screened in the 800−1800 °C and 100−130 MPa ranges, respectively. The uniaxial pressure was applied at room temperature and maintained constant while the sample was heated to the target temperature under argon at 100 °C·min^{-1}. The pressure was maintained for 1 min at the dwell temperature. The mechanical constraint was released at the end of the heat treatment, and the sample was then allowed to cool naturally to room temperature (RT). After a polishing step, cohesive pellets with different colors were recovered. Depending on the dwell temperature during

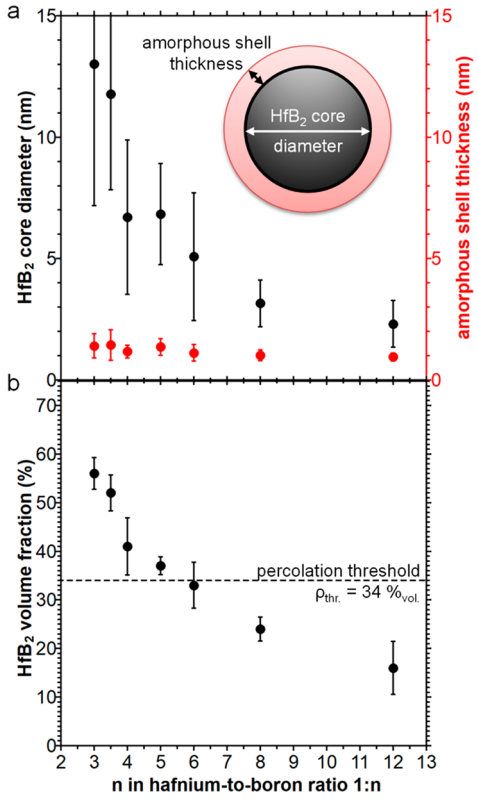

Figure 4. (a) Average core diameter and shell thickness of core−shell nanoparticles measured from TEM pictures including standard deviations. (b) Corresponding volume fraction ρ of HfB_2 cores in the nanocomposites as a function of the amount of boron precursor initially introduced. The theoretical percolation threshold (dashed line) represents the minimal volume fraction required for a monodisperse assembly of spheres to percolate within a three-dimensional space.

SPS, they are matte black after a treatment at 800 °C, brilliant black up to 1200 °C, and metallic gray for 1350 °C and above (Figure S3). Figure 5 displays the XRD patterns of the initial

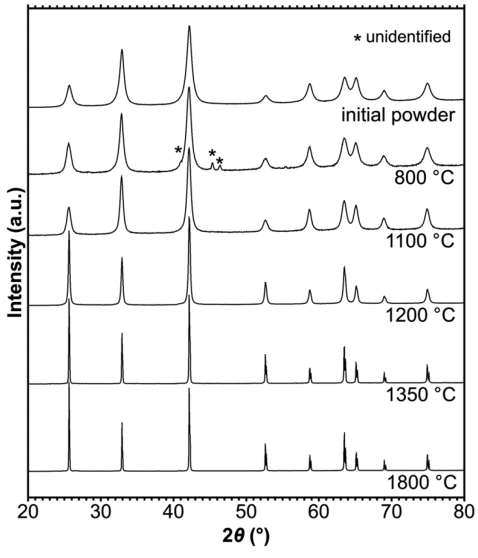

Figure 5. XRD patterns of the initial powder obtained with Hf:B = 1:4 and of pellets densified by SPS at various temperatures from 800 to 1800 °C under a uniaxial pressure of 100 MPa.

powder 1:4 and of samples sintered at 100 MPa and various temperatures. No reflection corresponding to crystalline boron could be detected. HfB_2 remains the only crystalline phase after SPS, except after sintering at 800 °C. This sample is contaminated with a minor unidentified phase, which is attributed to external contamination. With increasing sintering temperatures, XRD reflections sharpen due to crystal growth. The apparent crystallite size calculated using the Scherrer formula[63] shows a steep increase (Figure 6a) between 1200

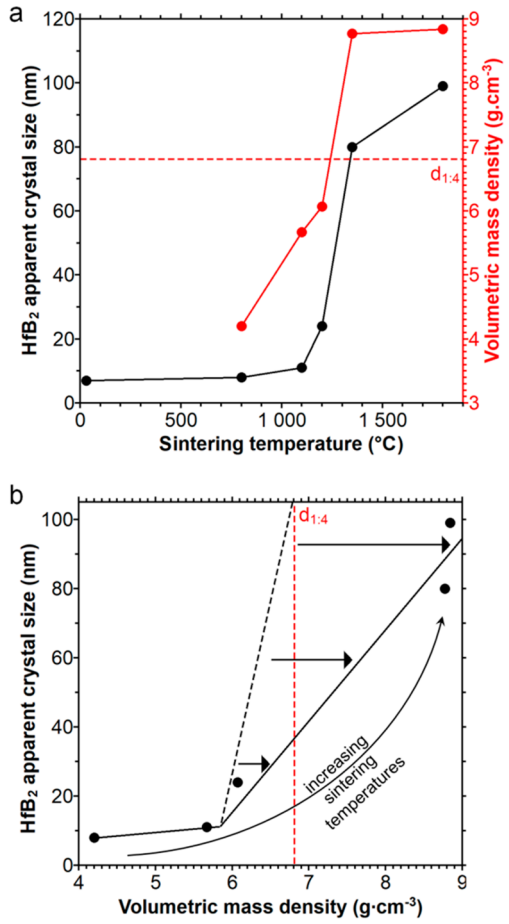

Figure 6. (a) HfB_2 crystallite size and volumetric mass density of pellets obtained by SPS of powders with an initial Hf:B molar ratio 1:4 under a uniaxial pressure of 100 MPa as a function of sintering temperature. (b) Crystal size as a function of pellet density. In the high density regime (high sintering temperature), values exceed the density of the initial powder $d_{1:4}$ (red solid line), denoting a deviation (black arrows) from the expected sintering behavior (black dashed line). Experimental data points are connected by guide-to-the-eye lines.

and 1350 °C from 24 to 80 nm. Above 1350 °C, the Scherrer formula reaches its limits of applicability, which is associated with the instrumental broadening for crystal growth above the nanometer size range.

The volumetric mass density of the pellets resulting from SPS was measured by hydrostatic pycnometry (Figure 6a). The density increases linearly up to 1200 °C and then increases abruptly before reaching a plateau at approximately 9 $g{\cdot}cm^{-3}$. Between 1200 and 1350 °C, the highest increase rate in density is accompanied by the highest rate in crystal growth. The apparent crystal size plotted as a function of density (Figure 6b) shows two successive regimes: densification with limited

crystal growth at low temperatures and densification accompanied by a stronger crystal growth at 1350 °C and above. The volumetric mass densities of pellets sintered at 1350 and 1800 °C (respectively 8.77 and 8.84 g·cm^{-3}) are approximately 30% higher than the volumetric mass density of the initial powder $d_{1:4}$ = 6.81 g·cm^{-3}, measured by helium pycnometry, which enables accessing open pores in the subnanometer range (kinetic diameter of 2.6 Å).[64] This high-temperature densification is unusual compared to a common behavior, indicated by a dotted black line, where the upper limit of the density of the pellet is expected to be the density of the powder measured by He pycnometry.[65] This behavior is reflected in the withdrawal of the piston mold during SPS (Figure S3): two successive shrinkages occur around 800 and 1000 °C for pellets sintered at 1100 and 1200 °C, which enable both densifying the material and keeping HfB_2 nanocrystals with only slight crystal growth (Figure 6). An additional shrinkage is observed above 1300 °C for pellets sintered at 1350 and 1800 °C (Figure S3). This high-temperature densification was further examined by analyzing the nanostructure of the SPS pellets using scanning electron microscopy (SEM).

The pellets were investigated from their basal surface (Figure S4) after polishing. Near-spherical nanoparticles with a diameter around 10 nm as in the initial 1:4 powder (Figure 2, Figure 7a) are maintained for the sample sintered at 1100 °C,

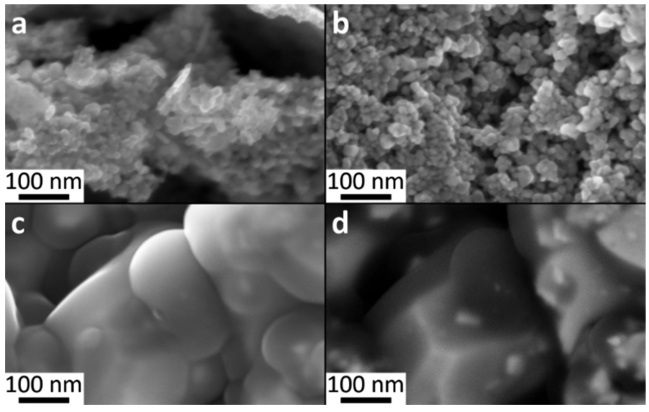

Figure 7. SEM-FEG micrographs of (a) the initial powder with the Hf:B molar ratio of 1:4, and the resulting pellets after SPS under 100 MPa at (b) 1100 °C and (c, d) 1800 °C. The exact same region is analyzed in (c) and (d). The images are acquired in (a–c) secondary electron and (d) backscattered electron modes.

as observed in scratched out areas in Figure 7b. The pellet obtained at 1800 °C is composed of particles with sizes between 50 nm and 1 μm (Figure 7c). Imaging in backscattered electron mode provides the chemical contrast between hafnium- and boron-rich regions, where dark contrast areas in Figure 7d (see also Figure S4c) are poor in hafnium and rich in light elements, assigned to boron, while bright particles are assigned to HfB_2. Therefore, the nanostructure of the powder constituted of 10 nm core–shell nanoparticles is maintained at 1100 °C but turns into a dense mixture of HfB_2 and boron-rich submicrometer particles after sintering at 1800 °C: elemental heterogeneity is observed at the submicrometer scale. Not only do HfB_2 nanocrystals grow during SPS at 1800 °C, but elemental segregation also occurs in the boron-rich amorphous matrix. Overall, a sintering temperature below 1200 °C is necessary to prevent the sample from elemental segregation and to ensure a preserved nanostructure.

The high-temperature densification phenomenon observed above 1200 °C is accompanied by extensive crystal growth and a large increase of the pellet density above the He pycnometry-measured density of the pristine powder. By considering that the composite is made of HfB_2 (11.21 g·cm^{-3})[52] and boron (2.37 g·cm^{-3})[31] with the overall Hf:B ratio measured by EDS, we evaluate the expected density d_{thr} to 9.21 g·cm^{-3} (calculation detailed in the Experimental Section). After the high-temperature densification event (Figure 6b), the pellet densities are 8.75 and 8.84 g·cm^{-3} at 1350 and 1800 °C, respectively. These values represent 95 and 96% of d_{thr}, respectively. According to XRD, SEM, and density measurements, the high temperature pellets obtained above 1350 and 1800 °C are then consistent with HfB_2 and amorphous boron submicrometer particles. The HfB_2 phase is maintained at all temperatures, which is in agreement with its refractory properties.[53,54]

The calculations presented above show that the density $d_{1:4}$ of the pristine sample at room temperature is inconsistent with a sample made of HfB_2 and reported amorphous boron.[31,52] Because the HfB_2 structure is verified by XRD, the observed deviation of the density versus the ideal case must relate to the amorphous shell. Taking into account the density of boron oxide or boric acid to correct for the oxidized fraction of boron in the shell cannot explain the surprisingly low density of the 1:4 powder. Hence, the $d_{1:4}$ value can be explained either by closed pores that cannot be probed by helium pycnometry or by a local structure different than those tabulated for amorphous boron. The hypothesis of closed porosity can be discarded because such pores would be filled with salts from the synthesis or deionized water from the washing step, while none of these species could be detected in sufficient amounts to explain the density values (EDS does not show any salt and the oxygen content is not consistent with 30 wt % of water needed to reach such low density values). Therefore, we propose that the initial amorphous shell embedding the HfB_2 nanoparticles in the pristine powder is constituted of a low-density form of partially oxidized elemental boron. Further efforts will be needed in the future to investigate the structural features of this elemental boron form. ^{11}B NMR and XPS data suggest that oxidized boron species are already chemically similar to borates.[43,46] Partial oxidation of the initial amorphous shell is supported by the observation that the low temperature sintering events at 800–900 °C are accompanied by the formation of a white deposit on the outer parts of the mold, typical of boron oxide, which is volatile in the conditions of SPS sintering.[46,66,67] We hypothesize that oxidized boron species are eliminated during SPS, yielding a nanocomposite of HfB_2 and elemental amorphous boron.

While the amorphous component is constituted of common elemental boron above 1350 °C and by a low density form in the initial powder, the nature of this amorphous component must be questioned for the low temperature pellets obtained at 800, 1100, and 1200 °C. The high-temperature densification event is accompanied by elemental segregation leading to the loss of core–shell architecture, large HfB_2 grain growth, and amorphous submicrometer boron particles. These abrupt changes suggest a correlation to structural transformations in the amorphous component and thus suggest that the samples sintered at lower temperature still encompass the low-density form detected in the powder at room temperature. This

hypothesis is supported by the only slight particle growth occurring during sintering at these temperatures, which shows that no extensive restructuration has taken place. Likewise, these low-temperature pellets are cohesive, and the samples obtained at 1100 and 1200 °C exhibit bright faces and only a few pores according to SEM (Figure S4), showing efficient densification. Therefore, by taking into account the density of the initial powder 1:4, the 800, 1100, and 1200 °C pellets correspond to a densification of 62, 83 and 89%, respectively (Table 1).

Table 1. HfB_2 Apparent Crystal Size and Density of Pellets Sintered from Two Boron-Rich Nanocomposites (Hf:B) under Various Sintering Pressures (P) and Temperatures (T)

sample Hf:B-T (°C)-P (MPa)	HfB_2 size (nm)	volumetric mass density ($g{\cdot}cm^{-3}$)	relative density (%)
1:4[a]	7	6.81	X
1:6[a]	5	4.12	X
1:4-800-100	8	4.20	62
1:4-1100-100	11	5.67	83
1:4-1100-130	18	6.02	88
1:4-1200-100	24	6.07	89
1:6-1200-100	9	4.27	103

[a]Pristine powders.

In order to maintain the nanostructure in the composite, the sintering temperature was restricted to 1200 °C. The role of the hafnium-to-boron molar ratio and of the sintering pressure on the final density and the particle size was further studied. Table 1 displays crystallite sizes calculated from XRD patterns (Figure S5) using the Scherrer formula, volumetric mass densities, and relative densities, using the experimental density of pristine powder samples 1:4 and 1:6 as references. Note that the apparent crystal sizes derived by XRD in the pristine powders are consistent with TEM analysis of HfB_2 core diameters (Figure 4a). The pellet sintered from powder 1:4 at 1100 °C and 100 MPa (1:4-1100-100) is compared to the sample 1:4-1100-130. An increase in sintering pressure from 100 to 130 MPa improves the density from 83 to 88% with a limited crystal growth from 11 to 18 nm. The pristine powder 1:6 treated at 1200 °C and 100 MPa (1:6-1200-100) yields crystal growth from 5 to 9 nm (+80%). This is a limited change relatively to the sample 1:4-1200-100 (7 to 24 nm, i.e., +340%). This difference is attributed to a higher volume fraction of amorphous matrix, i.e., more diluted nanocrystal dispersion: confinement of HfB_2 nanocrystals slows down their growth. The relative density above 100% for the sample 1:6-1200-100 suggests that restructuration also started in the amorphous shell.

Three nanostructured pellets have been obtained with densities ranging from 88 to 100%: 1:4-1100-130, 1:4-1200-100, and 1:6-1200-100. These values are adequate for the study of transport properties, including electrical and thermal properties. Dense ceramics with two HfB_2 volumetric ratios (above and around the percolation threshold) are also relevant for studying the impact of the composition of the nanocomposite on transport properties.

Tuning Transport Properties. Electrical and thermal conductivities of the 1:4-1100-130, 1:4-1200-100, 1:6-1200-100, and 1:4-1350-100 samples are reported as a function of temperature in Figure 8. Corrections from porosity effects were applied following the Maxwell−Eucken equation (details can

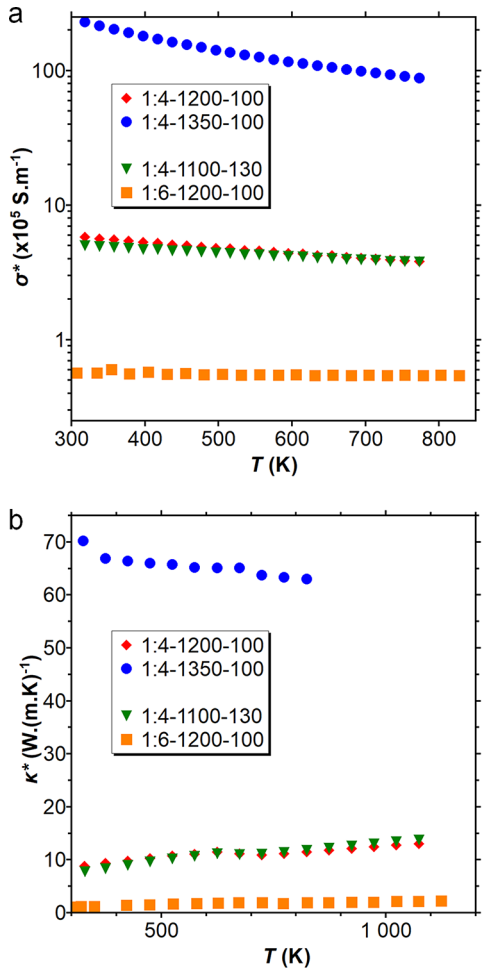

Figure 8. Thermal dependence of (a) electrical and (b) thermal conductivities in boron-rich dense nanocomposites (Hf:B-T (°C)-P (MPa)). The values are corrected from the contribution of pores by using the Maxwell−Eucken equation.

be found in the Experimental Section). Electrical and thermal conductivities vary by ca. 2 orders of magnitude, depending on the initial hafnium-to-boron ratio and sintering conditions. We focus first on samples with an Hf:B initial ratio of 1:4 at 100 MPa. After sintering at 1350 °C, both conductivity values ($9 \times 10^6 < \sigma^* < 2.3 \times 10^7$ $S{\cdot}m^{-1}$ and $63 < \kappa^* < 70$ $W{\cdot}m^{-1}{\cdot}K^{-1}$) and their thermal dependence between room temperature and 700 K are similar to those of bulk HfB_2 ($6.7 \times 10^6 < \sigma^* < 1.7 \times 10^7$ $S{\cdot}m^{-1}$ and $70 < \kappa^* < 100$ $W{\cdot}m^{-1}{\cdot}K^{-1}$),[52,59] indicating a metallic behavior consistent with the large HfB_2 grain growth described above. The metallic behavior is also observed after sintering at 1800 °C (Figure S6). Decreasing the sintering temperature down to 1200 °C leads to a decrease of both electrical and thermal conductivities by 1 order of magnitude. The thermal dependence of the thermal conductivity corrected from porosity (κ^*) changes drastically and especially deviates from bulk HfB_2.[59] The electrical conductivity corrected from porosity (σ^*) is around 4×10^5 $S{\cdot}m^{-1}$ and still shows a metallic temperature dependence, suggesting that the decrease in conductivity with the decrease of the sintering temperature from 1350 to 1200 °C originates from fewer electronic

percolation paths between HfB_2 nanocrystals, in agreement with their smaller particle size. Decreasing the sintering temperature further from 1200 to 1100 °C leads to a decrease in electrical conductivity by 1 order of magnitude and no significant temperature dependence. This low electrical conductivity is in agreement with smaller HfB_2 nanocrystals and inefficient percolation of conduction paths. Furthermore, an increase of the pressure from 100 to 130 MPa enables recovering at low sintering temperature (1:4-1100-130) the transport properties of a higher temperature pellet at 100 MPa (1:4-1200-100), in agreement with their similar nanostructures. Finally, increasing the boron content from 1:4 (1:4-1200-100) to 1:6 (1:6-1200-100) leads to electrical and thermal conductivities decreased by 1 order of magnitude, in agreement with the higher volume fraction of the electrically and thermally insulating matrix. Overall high HfB_2-related electrical conductivities in the 0.4×10^5–4×10^5 $S \cdot m^{-1}$ range are maintained in the nanocomposites, accompanied by low thermal conductivities in the 1–10 $W \cdot m^{-1} \cdot K^{-1}$ range. Thermal conductivity switches from a metallic behavior when the HfB_2 size is on the submicrometer size range and amorphous boron is segregated, to a nonmetallic one when the nanocomposite is maintained for low sintering temperatures.

Seebeck coefficients S measured as a function of temperature (Figure 9) are negative, indicating that electrons are the

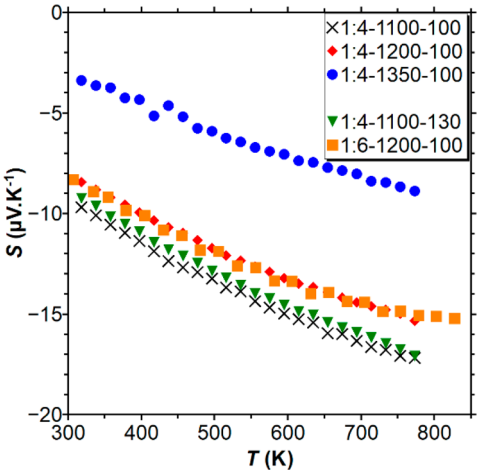

Figure 9. Thermal dependence of Seebeck coefficient in boron-rich dense nanocomposites (Hf:B-T (°C)-P (MPa)).

majority carrier type as expected from the metallic conductivity. Accordingly, sintering above 1350 °C yields S values typical for metals.[68,69] Absolute S values at RT are approximately three times larger in samples sintered at 1200 °C and below. They also increase when lowering the temperature of sintering from 1200 to 1100 °C, showing a larger contribution of the insulating matrix, as expected from the maintained nanostructure. As long as the nanostructure is kept in the composite, the Seebeck coefficient is independent of the sintering pressure and the Hf:B ratio. Low S values result in low thermoelectric figures of merit ZT of ca. 0.01 at 1000 K calculated by extrapolating σ and S dependences with the temperature. These modest values are not surprising given that HfB_2 systematically rules over the electrical behavior, even for a relatively high content of amorphous boron matrix. The samples all exhibit pronounced metallic behavior evidenced by electrical conductivity and Seebeck coefficient measurements. On the contrary, the thermal conduction behavior in nanocomposites is changed compared to the bulk sample, suggesting that it is impacted by the amorphous matrix.

Although the Seebeck coefficient is low, it is informative to highlight the ability to decouple the electrical σ and thermal κ conductivities by calculating the σ/κ ratio (Table 2). Bulk

Table 2. Transport Properties at 1000 K[a] of Boron-Rich Dense Nanocomposites and Some Other Boron-Based Materials from Literature

sample Hf:B-T (°C)-P (MPa)	type	κ ($W \cdot m^{-1} \cdot K^{-1}$)	σ ($S \cdot m^{-1}$)	σ/κ ($S \cdot K \cdot W^{-1}$)
1:4-1200-100	n	12.8	2.8×10^5	3.3×10^4
1:4-1100-130	n	13.4	2.7×10^5	3.7×10^4
1:6-1200-100	n	2.1	5.5×10^4	2.8×10^4
β-B[60]	p	10	1.0×10^3	1.0×10^2
Hfb_2[52,59]	n	100	5×10^6	5×10^4
$B_{6.5}C$[27,a]	p	3.0	5.0×10^4	1.7×10^4
$Yb_{66}C_{0.6}$[55]	p	1.5	250	1.7×10^2
$Erb_{44}Si_2$[70]	p	1.6	1.4×10^3	8.8×10^2
$Ca_{0.5}Sr_{0.5}B_6$[28]	n	8.9	1.0×10^5	1.1×10^4
$Hob_{17}Cn$[71]	n	1.7	1.1	0.6

[a] 1250 K for $B_{6.5}C$.

HfB_2 and β-B references provide benchmarks to address the properties of the nanocomposites we designed. A large increase in σ/κ by 2 orders of magnitude is observed when compared to β-B, due to enhanced electrical conductivity, whereas the thermal conductivities are similar. σ/κ values of the nanocomposites are similar to those of bulk HfB_2, but they reflect a 2 orders of magnitude decrease of both σ and κ in the case of the sample 1:6-1200-100. The deteriorated metallic behavior compared to that of bulk HfB_2 is a prerequisite to improved thermoelectric properties. The electrical conductivitiy of sample 1:6-1200-100 is indeed comparable to those of reference boron-rich thermoelectric materials (Table 2), despite being composed of a large fraction of metallic HfB_2 (33 vol %). The overall ratio σ/κ is higher than most boron-based materials scrutinized for their thermoelectric properties, thus showing the large decoupling of electrical and thermal properties achieved in the nanocomposites. The nanocomposites have unusual transport properties combining electrical metallic behavior associated with HfB_2 nanocrystals and thermal insulating properties common to boron-rich phases.

The sample 1:4 synthesized with a large HfB_2 volume fraction (41 vol %) above the percolation threshold expectedly shows electrical properties driven by the metallic HfB_2 component but with a lower κ attributed to the insulating boron-rich matrix and to phonon scattering by the nanostructure. The similar behavior of the sample 1:6 despite being at the edge of the percolation threshold after synthesis may be related to the loss of volatile components from the initial amorphous shell. This evolution yields an increase in the HfB_2 volume fraction, which may then reach values higher than the percolation ratio.

CONCLUSIONS

We have shown that synthesis in inorganic molten salts is a unique tool to enable the one-pot design of boron-based core–shell nanoparticles with an adjustable volume fraction of core and shell constituents. This versatility combined with the

efficiency of spark plasma sintering to yield dense monoliths while maintaining the size of nanoinclusions results in distinct electrical and thermal conductivities, with a strong decoupling between both transport properties. In addition, the sintering step evidences significant structural reorganization in an amorphous boron-rich component, which will be studied in the future. All in all, this work provides a new avenue for the future design of nanostructured monolithic boron-rich composites with tunable properties, encompassing electrical and thermal properties but also mechanical properties.

EXPERIMENTAL SECTION

Powder Synthesis. LiCl (99%), KCl (99%), $NaBH_4$ (98%), and anhydrous $HfCl_4$ (99.9%) were purchased from Alfa Aesar. In an argon-filled glovebox (MBraun), boron and hafnium precursors were added to a mixture of LiCl/KCl at the eutectic composition (45/55 wt %) previously dried under a vacuum at 200 °C during 48 h. For each synthesis, the quantities used are reported in Table S1. The mixture was ball milled for 2 min at 20 Hz using a MM400 (Retsch) container and stainless-steel balls. The resulting powder was transferred in a glassy carbon crucible, and the crucible was maintained in a quartz tube. The setup was connected to an argon ramp. The reaction medium was heated to 900 °C in a vertical oven (Carbolite) for 4 h after a 10 °C·min^{-1} ramp from RT. The medium was mixed during the experiment, using a glassy carbon rod rotating at approximately 120 rpm. After heating, the medium was left to cool naturally to RT. Under air, the solidified salt medium was washed three times by successive dispersion in deionized water, sonicated for few minutes in an USC100TH (VWR) ultrasonic bath, and centrifuged for 15 min at 22 to 26 krpm (Sigma 3-30k), and the supernatant was discarded. The black powder was dried under vacuum overnight at 60 °C and stored under air. Up to 400 mg of powder is obtained per synthesis.

Spark Plasma Sintering. Spark plasma sintering experiments were performed on a 515S Syntex (Dr. Sinter) apparatus. In a typical procedure, 1 g of HfB_2-based nanocomposite was introduced in a graphite die (inner diameter of 8 mm) covered with Papyex. The SPS chamber was maintained under an argon flow at 1 atm during the experiment. The uniaxial pressure of 5 kN (100 MPa) or 6.5 kN (130 MPa) was applied at 0.5 kN·min^{-1} prior to heating at 600 °C. A heating ramp of 100 °C·min^{-1} was then applied up to temperatures ranging from 800 to 1800 °C (107 °C·min^{-1} for 1350 °C). The sample was maintained for 1 min at the dwell temperature. The pressure was released to 0.5 kN (minimal charge) in 3 min, and the apparatus cooled naturally under argon in 20 min. A polishing step was required to remove the carbon layer from Papyex, using abrasive SiC sandpapers with increasing grit sizes from 120 to 1200.

Transmission Electron Microscopy (TEM). A 120 kV Tecnai Spirit microscope was used for TEM and selected area electron diffraction (SAED) pictures. High resolution-TEM (HRTEM) was also operated on a 200 kV JEOL JEM 2011 apparatus, at the Institut des Matériaux de Paris Centre. Samples were prepared by evaporating a drop of suspension in ethanol on a carbon-coated copper grid. Core and shell size distributions were obtained from measurements on at least 100 particles with pictures from three different regions of the grid. For simplicity, the HfB_2 volume fraction is calculated from the average core diameter and shell thickness measurements. The SAED pattern was indexed along the HfB_2 structure (ICDD file 00-038-1398).

X-ray Diffraction (XRD). Measurements were performed on a D8 Bruker apparatus operating at the Cu $K\alpha_1/K\alpha_2$ radiations, acceleration tension of 45 kV, working current of 40 mA, $10 \leq 2\theta \leq 80°$ with 0.05° steps, and counting time of 2 s per step. Patterns were indexed according to the ICDD files: HfB_2 (00-038-1398) and HfO_2 (00-043-1017). Apparent crystallite sizes ε were calculated using the Scherrer formula and pseudo-Voigt functions to fit peaks. Le Bail refinements were performed on JANA2006 software.[72]

Scanning Electron Microscopy (SEM) and Energy Dispersive X-ray Spectrometry (EDS). A SU-70 (Hitachi) field emission SEM operating at 5 kV was used for imaging powders deposited on conductive and adhesive tape. Pellets were observed from their basal surfaces. Samples were covered with a carbon layer of approximately 20 nm by thermal evaporation. Energy dispersive X-ray analyses were performed with a S-3400-N (Hitachi) SEM operating at 10 kV and equipped with an X-Max EDS system (Oxford Instruments) utilizing a large area (20 mm^2) analytical silicon drift EDS detector. The beam current was measured in order to test the quality of the spectra to be quantified. X-ray lines used for quantification were B K, O K, and Hf M. The quantitative data are the average of four measurements in different regions. Elemental composition of pristine powder with standard deviations: Hf: 20(2) atom %; B: 63(1) atom %; O: 17(2) atom %.

Inductive Coupled Plasma–Optical Emission Spectrometry. ICP-OES measurements were acquired on an iCAP 6000 apparatus (ThermoFischer). The hafnium diboride powder was dissolved in a 5 mol·L^{-1} nitric acid solution. Each elemental concentration shown is the average of three measurements.

Volumetric Mass Density. For pellets, the volumetric mass density was calculated from hydrostatic pycnometry consisting of three mass measurements of the pellet (i) dried, (ii) immerged in deionized water at 25 °C, and (iii) wet with excess water removed with a tissue. Helium pycnometry was performed to measure the density of powders, using a Ultrapyc 1200e (Quantachrome Corporation).

Calculation of the Maximal Density Expected for Pellets Sintered at 1350 °C and above (d_{thr}). For calculating d_{thr}, we considered a composite made of HfB_2 ($d(HfB_2)$ = 11.21 g·cm^{-3})[52] and amorphous boron ($d(B)$ = 2.37 g·cm^{-3}).[31] The specific volume of the composite is the volume occupied by the HfB_2 component added to the volume of amorphous boron for 1 g of composite:

$$V = \frac{m(HfB_2)}{d(HfB_2)} + \frac{m(B)}{d(B)}$$

EDS measurements on the pellets sintered at 1350 and 1800 °C indicated a B/Hf molar ratio of 3:1. From this ratio we deduced that 65 atom % of boron is in HfB_2 and the remaining 35 atom % is in the shell. The proportions of the two phases are then 94.2 wt % of HfB_2 and 5.8 wt % of B. Then, the specific volume of the composite is V = 0.108 cm^{-3}·g^{-1}, which corresponds to a density d_{thr} = 9.21 g·cm^{-3}.

Thermal Conductivity. Thermal conductivity was measured on cylindrical pellets, 8.0 mm in diameter and 1.2 to 3.0 mm thick, under nitrogen (20 mL·min^{-1}), using a Laser Flash Apparatus 457 MicroFlash (Netzsch) at 1054 nm and equipped with an InSb infrared detector. At each temperature, three consecutive measurements were averaged. Calorific capacities per unit mass were calculated as a function of temperature from the tabulated molar calorific capacities of hafnium diboride and elemental boron (beta) accessible on the National Institute of Standards and Technology database,[73] taking mass fractions of the composite into account. Porosity has an effect on transport properties such as electrical (σ) and thermal (κ) conductivities. The contribution of pores can be deduced using the Maxwell–Eucken equation, giving access to the corrected values of conductivity t^*:

$$t^* = t\frac{1 + \beta P}{1 - P}$$

t is either σ or κ, the porosity P delineates a limit of application of the equation with P_{max} = 0.2, and β is an empirical form factor that reflects the influence of the pore geometry. It ranges from 1 to 3 and is fixed at 2, as reported in other studies with similar geometries.[18,27,74] Accordingly, the correction factor ranges from 1 for a fully densified pellet to 1.75 for P_{max} = 0.2.

Seebeck Coefficient and Electrical Conductivity. The Seebeck coefficient and electrical conductivity were measured on rectangular rods shaped with a Isomet 5000 (Buehler) circular saw, using a ZEM-3 (ULVAC-RIKO) apparatus. At each temperature, one

measurement was performed with $\Delta T = 0$ for resistivity measurements, followed by three measurements with $\Delta T \neq 0$ for Seebeck measurements. The porosity effect on the electrical conductivity has been evaluated the same way as for thermal conductivity, detailed above.

Supporting Information

Table S1 summarizing synthesis conditions, Table S2 reporting HfB_2 cell parameters, and Figures S1 −S6 for additional characterization (PDF)

Corresponding Author

David Portehault − *Sorbonne Université, CNRS, Collège de France, Laboratoire Chimie de la Matière Condensée de Paris, LCMCP, F-75005 Paris, France;* orcid.org/0000-0003-4914-4913; Email: david.portehault@sorbonne-universite.fr

Authors

Guillaume Gouget − *Sorbonne Université, CNRS, Collège de France, Laboratoire Chimie de la Matière Condensée de Paris, LCMCP, F-75005 Paris, France;* orcid.org/0000-0002-6446-001X

Damien Bregiroux − *Sorbonne Université, CNRS, Collège de France, Laboratoire Chimie de la Matière Condensée de Paris, LCMCP, F-75005 Paris, France*

Rémi Grosjean − *Sorbonne Université, CNRS, Collège de France, Laboratoire Chimie de la Matière Condensée de Paris, LCMCP, F-75005 Paris, France; Sorbonne Université, CNRS, MNHN, IRD, Institut de Minéralogie, de Physique des Matériaux et de Cosmochimie, IMPMC, F-75005 Paris, France*

David Montero − *Sorbonne Université CNRS, Institut des Matériaux de Paris Centre, IMPC, F-75005 Paris, France*

Stefan Maier − *Laboratoire CRISMAT UMR 6508 CNRS ENSICAEN, 14050 Cedex 04 Caen, France*

Franck Gascoin − *Laboratoire CRISMAT UMR 6508 CNRS ENSICAEN, 14050 Cedex 04 Caen, France;* orcid.org/0000-0002-9791-1358

Clément Sanchez − *Sorbonne Université, CNRS, Collège de France, Laboratoire Chimie de la Matière Condensée de Paris, LCMCP, F-75005 Paris, France;* orcid.org/0000-0002-6426-4844

ACKNOWLEDGMENTS

The authors acknowledge Benjamin Villeroy from the Institut de Chimie de Matériaux Paris-Est for his help for helium pycnometry. This work was funded by the Ministère de l'Enseignement Supérieure et de la Recherche and the CNRS. The authors also thank Sorbonne Université and C'Nano projects of the Région Ile-de-France for additional funding.

REFERENCES

(1) Liu, X.; Deng, Y. D.; Li, Z.; Su, C. Q. Performance Analysis of a Waste Heat Recovery Thermoelectric Generation System for Automotive Application. *Energy Convers. Manage.* **2015**, *90*, 121−127.

(2) Zhang, J.; Xuan, Y.; Yang, L. Performance Estimation of Photovoltaic−Thermoelectric Hybrid Systems. *Energy* **2014**, *78*, 895−903.

(3) Sootsman, J. R.; Chung, D. Y.; Kanatzidis, M. G. New and Old Concepts in Thermoelectric Materials. *Angew. Chem., Int. Ed.* **2009**, *48* (46), 8616−8639.

(4) Chester, G. V.; Thellung, A. The Law of Wiedemann and Franz. *Proc. Phys. Soc., London* **1961**, *77* (5), 1005−1013.

(5) DiSalvo, F. J. Thermoelectric Cooling and Power Generation. *Science* **1999**, *285* (5428), 703−706.

(6) Liu, Z.; Mao, J.; Liu, T.-H.; Chen, G.; Ren, Z. Nano-Microstructural Control of Phonon Engineering for Thermoelectric Energy Harvesting. *MRS Bull.* **2018**, *43* (3), 181−186.

(7) Mori, T. Novel Principles and Nanostructuring Methods for Enhanced Thermoelectrics. *Small* **2017**, *13* (45), 1702013.

(8) He, J.; Tritt, T. M. Advances in Thermoelectric Materials Research: Looking Back and Moving Forward. *Science* **2017**, *357* (6358), eaak9997.

(9) Venkatasubramanian, R.; Siivola, E.; Colpitts, T.; O'Quinn, B. Thin-Film Thermoelectric Devices with High Room-Temperature Figures of Merit. *Nature* **2001**, *413* (6856), 597−602.

(10) Tang, X.; Xie, W.; Li, H.; Zhao, W.; Zhang, Q.; Niino, M. Preparation and Thermoelectric Transport Properties of High-Performance p-Type Bi_2Te_3 with Layered Nanostructure. *Appl. Phys. Lett.* **2007**, *90* (1), 012102.

(11) Kulbachinskii, V. a.; Kytin, V. G.; Popov, M. Y.; Buga, S. G.; Stepanov, P. B.; Blank, V. D. Composites of $Bi_{(2-x)}Sb_xTe_3$ Nanocrystals and Fullerene Molecules for Thermoelectricity. *J. Solid State Chem.* **2012**, *193*, 64−70.

(12) Hsu, K. F.; Loo, S.; Guo, F.; Chen, W.; Dyck, J. S.; Uher, C.; Hogan, T.; Polychroniadis, E. K.; Kanatzidis, M. C. Cubic $AgPb_mSbTe_{(2+m)}$: Bulk Thermoelectric Materials with High Figure of Merit. *Science* **2004**, *303* (5659), 818−821.

(13) Sootsman, J. R.; Pcionek, R. J.; Kong, H.; Uher, C.; Kanatzidis, M. G. Strong Reduction of Thermal Conductivity in Nanostructured PbTe Prepared by Matrix Encapsulation. *Chem. Mater.* **2006**, *18* (21), 4993−4995.

(14) Sootsman, J. R.; Kong, H.; Uher, C.; D'Angelo, J. J.; Wu, C. I.; Hogan, T. P.; Caillat, T.; Kanatzidis, M. G. Large Enhancements in the Thermoelectric Power Factor of Bulk PbTe at High Temperature by Synergistic Nanostructuring. *Angew. Chem., Int. Ed.* **2008**, *47* (45), 8618−8622.

(15) Hao, Q.; Zhu, G.; Joshi, G.; Wang, X.; Minnich, A.; Ren, Z.; Chen, G. Theoretical Studies on the Thermoelectric Figure of Merit of Nanograined Bulk Silicon. *Appl. Phys. Lett.* **2010**, *97* (6), 063109.

(16) Dresselhaus, M. S.; Chen, G.; Tang, M. Y.; Yang, R.; Lee, H.; Wang, D.; Ren, Z.; Fleurial, J. P.; Gogna, P. New Directions for Low-Dimensional Thermoelectric Materials. *Adv. Mater.* **2007**, *19* (8), 1043−1053.

(17) Kovalenko, M. V.; Spokoyny, B.; Lee, J.-S.; Scheele, M.; Weber, A.; Perera, S.; Landry, D.; Talapin, D. V. Semiconductor Nanocrystals Functionalized with Antimony Telluride Zintl Ions for Nanostructured Thermoelectrics. *J. Am. Chem. Soc.* **2010**, *132* (19), 6686−6695.

(18) Ibáñez, M.; Zamani, R.; Gorsse, S.; Fan, J.; Ortega, S.; Cadavid, D.; Morante, J. R.; Arbiol, J.; Cabot, A. Core−Shell Nanoparticles As Building Blocks for the Bottom-Up Production of Functional Nanocomposites: PbTe−PbS Thermoelectric Properties. *ACS Nano* **2013**, *7* (3), 2573−2586.

(19) See, K. C.; Feser, J. P.; Chen, C. E.; Majumdar, A.; Urban, J. J.; Segalman, R. A. Water-Processable Polymer-Nanocrystal Hybrids for Thermoelectrics. *Nano Lett.* **2010**, *10* (11), 4664−4667.

(20) Yu, C.; Kim, Y. S.; Kim, D.; Grunlan, J. C. Thermoelectric Behavior of Segregated-Network Polymer Nanocomposites. *Nano Lett.* **2008**, *8* (12), 4428−4432.

(21) Dismukes, J. P.; Ekstrom, L.; Steigmeier, E. F.; Kudman, I.; Beers, D. S. Thermal and Electrical Properties of Heavily Doped Ge-Si Alloys up to 1300 K. *J. Appl. Phys.* **1964**, *35* (10), 2899.
(22) Wood, C. Materials for Thermoelectric Energy Conversion. *Rep. Prog. Phys.* **1988**, *51*, 459.
(23) Brown, S. R.; Kauzlarich, S. M.; Gascoin, F.; Snyder, G. J. $Yb_{14}MnSb_{11}$: New High Efficiency Thermoelectric Material for Power Generation. *Chem. Mater.* **2006**, *18* (7), 1873−1877.
(24) Chamoire, A.; Gascoin, F.; Estournès, C.; Caillat, T.; Tédenac, J.-C. High-Temperature Transport Properties of $Yb_{4-x}Sm_xSb_3$. *J. Electron. Mater.* **2010**, *39* (9), 1579−1582.
(25) Chamoire, A.; Gascoin, F.; Estournès, C.; Caillat, T.; Tédenac, J.-C. High-Temperature Transport Properties of Complex Anti-monides with Anti-Th_3P_4 Structure. *Dalt. Trans.* **2010**, *39* (4), 1118−1123.
(26) May, A. F.; Fleurial, J.-P.; Snyder, G. J. Thermoelectric Performance of Lanthanum Telluride Produced via Mechanical Alloying. *Phys. Rev. B: Condens. Matter Mater. Phys.* **2008**, *78* (12), 125205.
(27) Bouchacourt, M.; Thevenot, F. The Correlation between the Thermoelectric Properties and Stoichiometry in the Boron Carbide Phase B_4C-$B_{10.5}C$. *J. Mater. Sci.* **1985**, *20* (4), 1237−1247.
(28) Takeda, M.; Terui, M.; Takahashi, N.; Ueda, N. Improvement of Thermoelectric Properties of Alkaline-Earth Hexaborides. *J. Solid State Chem.* **2006**, *179* (9), 2823−2826.
(29) Gürsoy, M.; Takeda, M.; Albert, B. High-Pressure Densified Solid Solutions of Alkaline Earth Hexaborides (Ca/Sr, Ca/Ba, Sr/Ba) and Their High-Temperature Thermoelectric Properties. *J. Solid State Chem.* **2015**, *221*, 191−195.
(30) Fahrenholtz, W. G.; Hilmas, G. E.; Talmy, I. G.; Zaykoski, J. A. Refractory Diborides of Zirconium and Hafnium. *J. Am. Ceram. Soc.* **2007**, *90* (5), 1347−1364.
(31) Albert, B.; Hillebrecht, H. Boron: Elementary Challenge for Experimenters and Theoreticians. *Angew. Chem., Int. Ed.* **2009**, *48* (46), 8640−8668.
(32) Mori, T. Perspectives of High-Temperature Thermoelectric Applications and p-Type and n-Type Aluminoborides. *JOM* **2016**, *68* (10), 2673−2679.
(33) Slack, G. A.; Morgan, K. E. Some Crystallography, Chemistry, Physics, and Thermodynamics of $B_{12}O_2$, $B_{12}P_2$, $B_{12}As_2$, and Related Alpha-Boron Type Crystals. *J. Phys. Chem. Solids* **2014**, *75* (9), 1054−1074.
(34) Mori, T.; Nishimura, T.; Schnelle, W.; Burkhardt, U.; Grin, Y. The Origin of the N-Type Behavior in Rare Earth Borocarbide $Y_{1-x}B_{28.5}C_4$. *Dalt. Trans.* **2014**, *43* (40), 15048−15054.
(35) Sauerschnig, P.; Vaney, J. B.; Michiue, Y.; Kouzu, K.; Yamasaki, T.; Okada, S.; Yoshikawa, A.; Shishido, T.; Mori, T. Thermoelectric and Magnetic Properties of Spark Plasma Sintered REB_{66} (RE = Y, Sm, Ho, Tm, Yb). *J. Eur. Ceram. Soc.* **2020**, *40* (10), 3585−3591.
(36) Werheit, H. Boron-Rich Solids: A Chance for High-Efficiency High-Temperature Thermoelectric Energy Conversion. *Mater. Sci. Eng., B* **1995**, *29* (1−3), 228−232.
(37) Innocent, J.-L.; Portehault, D.; Gouget, G.; Maruyama, S.; Ohkubo, I.; Mori, T. Thermoelectric Properties of Boron Carbide/HfB_2 Composites. *Mater. Renew. Sustain. Energy* **2017**, *6* (2), 6.
(38) Mori, T.; Hara, T. Hybrid Effect to Possibly Overcome the Trade-off between Seebeck Coefficient and Electrical Conductivity. *Scr. Mater.* **2016**, *111*, 44−48.
(39) Carenco, S.; Portehault, D.; Boissière, C.; Mézailles, N.; Sanchez, C. Nanoscaled Metal Borides and Phosphides: Recent Developments and Perspectives. *Chem. Rev.* **2013**, *113*, 7981−8065.
(40) Portehault, D.; Delacroix, S.; Gouget, G.; Grosjean, R.; Chan-Chang, T.-H.-C. Beyond the Compositional Threshold of Nanoparticle-Based Materials. *Acc. Chem. Res.* **2018**, *51* (4), 930−939.
(41) Jothi, P. R.; Yubuta, K.; Fokwa, B. P. T. A Simple, General Synthetic Route toward Nanoscale Transition Metal Borides. *Adv. Mater.* **2018**, *30*, 1704181.
(42) Mori, T. Thermoelectric and Magnetic Properties of Rare Earth Borides: Boron Cluster and Layered Compounds. *J. Solid State Chem.* **2019**, *275*, 70−82.
(43) Portehault, D.; Devi, S.; Beaunier, P.; Gervais, C.; Giordano, C.; Sanchez, C.; Antonietti, M. A General Solution Route toward Metal Boride Nanocrystals. *Angew. Chem., Int. Ed.* **2011**, *50* (14), 3262−3265.
(44) Gouget, G.; Beaunier, P.; Portehault, D.; Sanchez, C. New Route toward Nanosized Crystalline Metal Borides with Tunable Stoichiometry and Variable Morphologies. *Faraday Discuss.* **2016**, *191*, 511−525.
(45) Gouget, G.; Debecker, D. P.; Kim, A.; Olivieri, G.; Gallet, J.-J.; Bournel, F.; Thomas, C.; Ersen, O.; Moldovan, S.; Sanchez, C.; Carenco, S.; Portehault, D. In Situ Solid−Gas Reactivity of Nanoscaled Metal Borides from Molten Salt Synthesis. *Inorg. Chem.* **2017**, *56* (15), 9225−9234.
(46) Grosjean, R.; Le Godec, Y.; Delacroix, S.; Gouget, G.; Beaunier, P.; Ersen, O.; Ihiawakrim, D.; Kurakevych, O. O.; Chanéac, C.; Portehault, D. A High Pressure Pathway toward Boron-Based Nanostructured Solids. *Dalt. Trans.* **2018**, *47* (23), 7634−7639.
(47) Son, H.-W.; Berthebaud, D.; Yubuta, K.; Yoshikawa, A.; Shishido, T.; Suzuta, K.; Mori, T. New Synthesis Route for Complex Borides; Rapid Synthesis of Thermoelectric Yttrium Aluminoboride via Liquid-Phase Assisted Reactive Spark Plasma Sintering. *Sci. Rep.* **2020**, *10* (1), 8914.
(48) Portehault, D.; Maneeratana, V.; Candolfi, C.; Oeschler, N.; Veremchuk, I.; Grin, Y.; Sanchez, C.; Antonietti, M. Facile General Route toward Tunable Magnéli Nanostructures and Their Use as Thermoelectric Metal Oxide/Carbon Nanocomposites. *ACS Nano* **2011**, *5* (11), 9052−9061.
(49) Anselmi-Tamburini, U.; Garay, J. E.; Munir, Z. A.; Tacca, A.; Maglia, F.; Spinolo, G. Spark Plasma Sintering and Characterization of Bulk Nanostructured Fully Stabilized Zirconia: Part I. Densification Studies. *J. Mater. Res.* **2004**, *19* (11), 3255−3262.
(50) Wang, L.; Zhang, J.; Jiang, W. Recent Development in Reactive Synthesis of Nanostructured Bulk Materials by Spark Plasma Sintering. *Int. J. Refract. Hard Met.* **2013**, *39*, 103−112.
(51) Cadavid, D.; Ibáñez, M.; Anselmi-Tamburini, U.; Durá, O. J.; López de laTorre, M. A.; Cabot, A. Thermoelectric Properties of Bottom-up Assembled $Bi_2S_{(3-x)}Te_x$. *Int. J. Nanotechnol.* **2014**, *11*, 773.
(52) Zhang, L.; Pejaković, D. a.; Marschall, J.; Gasch, M. Thermal and Electrical Transport Properties of Spark Plasma-Sintered HfB_2 and ZrB_2 Ceramics. *J. Am. Ceram. Soc.* **2011**, *94* (8), 2562−2570.
(53) Anselmi-Tamburini, U.; Kodera, Y.; Gasch, M.; Unuvar, C.; Munir, Z. A.; Ohyanagi, M.; Johnson, S. M. Synthesis and Characterization of Dense Ultra-High Temperature Thermal Protection Materials Produced by Field Activation through Spark Plasma Sintering (SPS): I. Hafnium Diboride. *J. Mater. Sci.* **2006**, *41* (10), 3097−3104.
(54) Monteverde, F. Ultra-High Temperature HfB_2-SiC Ceramics Consolidated by Hot-Pressing and Spark Plasma Sintering. *J. Alloys Compd.* **2007**, *428* (1−2), 197−205.
(55) Mori, T.; Tanaka, T. Effect of Transition Metal Doping and Carbon Doping on Thermoelectric Properties of YB_{66} Single Crystals. *J. Solid State Chem.* **2006**, *179* (9), 2889−2894.
(56) Berthebaud, D.; Nishimura, T.; Mori, T. Thermoelectric Properties and Spark Plasma Sintering of Doped $YB_{22}C_2N$. *J. Mater. Res.* **2010**, *25* (04), 665−669.
(57) Maruyama, S.; Prytuliak, A.; Miyazaki, Y.; Hayashi, K.; Kajitani, T.; Mori, T. Al Insertion and Additive Effects on the Thermoelectric Properties of Yttrium Boride. *J. Appl. Phys.* **2014**, *115* (12), 123702.
(58) Gouget, G.; Debecker, D. P.; Kim, A.; Olivieri, G.; Gallet, J.-J.; Bournel, F.; Thomas, C.; Ersen, O.; Moldovan, S.; Sanchez, C.; Carenco, S.; Portehault, D. In Situ Solid-Gas Reactivity of Nanoscaled Metal Borides from Molten Salt Synthesis. *Inorg. Chem.* **2017**, *56* (15), 9225−9234.
(59) Wuchina, E.; Opeka, M.; Causey, S.; Buesking, K.; Spain, J.; Cull, A.; Routbort, J.; Guitierrez-Mora, F. Designing for Ultrahigh-Temperature Applications: The Mechanical and Thermal Properties

of HfB_2, HfC_x, HfN_x and αHf(N). *J. Mater. Sci.* **2004**, *39* (19), 5939–5949.
(60) Takeda, M.; Fukuda, T.; Domingo, F.; Miura, T. Thermoelectric Properties of Some Metal Borides. *J. Solid State Chem.* **2004**, *177* (2), 471–475.
(61) Berkemeier, F.; Voss, S.; Imre, Á. W.; Mehrer, H. Molar Volume, Glass-Transition Temperature, and Ionic Conductivity of Na- and Rb-Borate Glasses in Comparison with Mixed Na-Rb Borate Glasses. *J. Non-Cryst. Solids* **2005**, *351* (52–54), 3816–3825.
(62) Lorenz, C. D.; Ziff, R. M. Precise Determination of the Critical Percolation Threshold for the Three-Dimensional "Swiss Cheese" Model Using a Growth Algorithm. *J. Chem. Phys.* **2001**, *114* (8), 3659.
(63) Patterson, A. L. The Scherrer Formula for X-Ray Particle Size Determination. *Phys. Rev.* **1939**, *56* (10), 978–982.
(64) Nguyen, H. G. T.; Horn, J. C.; Bleakney, M.; Siderius, D. W.; Espinal, L. Understanding Material Characteristics through Signature Traits from Helium Pycnometry. *Langmuir* **2019**, *35* (6), 2115–2122.
(65) Munir, Z. A.; Anselmi-Tamburini, U.; Ohyanagi, M. The Effect of Electric Field and Pressure on the Synthesis and Consolidation of Materials: A Review of the Spark Plasma Sintering Method. *J. Mater. Sci.* **2006**, *41* (3), 763–777.
(66) Matkovich, V. I. *Boron and Refractory Borides*; Springer-Verlag, Berlin, 1977, 207–208.
(67) Son, H.-W.; Sauerschnig, P.; Berthebaud, D.; Mori, T. Rapid Synthesis of Thermoelectric $YB_{22}C_2N$ via Spark Plasma Sintering with Gas/Solid Reaction Technology. *J. Ceram. Soc. Jpn.* **2020**, *128* (4), 181–185.
(68) Slack, G. *CRC Handbook of Thermoelectrics*; CRC Press.; Rowe, D. M., Ed.; Boca Raton, FL, 1995, 407–440.
(69) Imai, Y.; Mukaida, M.; Ueda, M.; Watanabe, A. Screening of the Possible Boron-Based n-Type Thermoelectric Conversion Materials on the Basis of the Calculated Densities of States of Metal Borides and Doped β-Boron. *Intermetallics* **2001**, *9* (8), 721–734.
(70) Mori, T. Thermal Conductivity of a Rare-Earth -Icosahedral Compound. *Phys. B* **2006**, *383* (1), 120–121.
(71) Mori, T.; Nishimura, T. Thermoelectric Properties of Homologous P- and n-Type Boron-Rich Borides. *J. Solid State Chem.* **2006**, *179* (9), 2908–2915.
(72) Petrícek, V.; Dušek, M.; Palatinus, L. Crystallographic Computing System JANA2006: General Features. *Zeitschrift fur Krist.* **2014**, *229* (5), 345–352.
(73) Chase, M. W. NIST-JANAF Thermochemical Tables, 4th ed.; *Journal of Physical and Chemical Reference Data*; American Chemical Society and American Institute of Physics: 1998; Monogr. 9.
(74) Adachi, J.; Kurosaki, K.; Uno, M.; Yamanaka, S. Effect of Porosity on Thermal and Electrical Properties of Polycrystalline Bulk ZrN Prepared by Spark Plasma Sintering. *J. Alloys Compd.* **2007**, *432* (1–2), 7–10.